Joule

CellPress

Article

How Surface Orientation Affects Jumping-Droplet Condensation

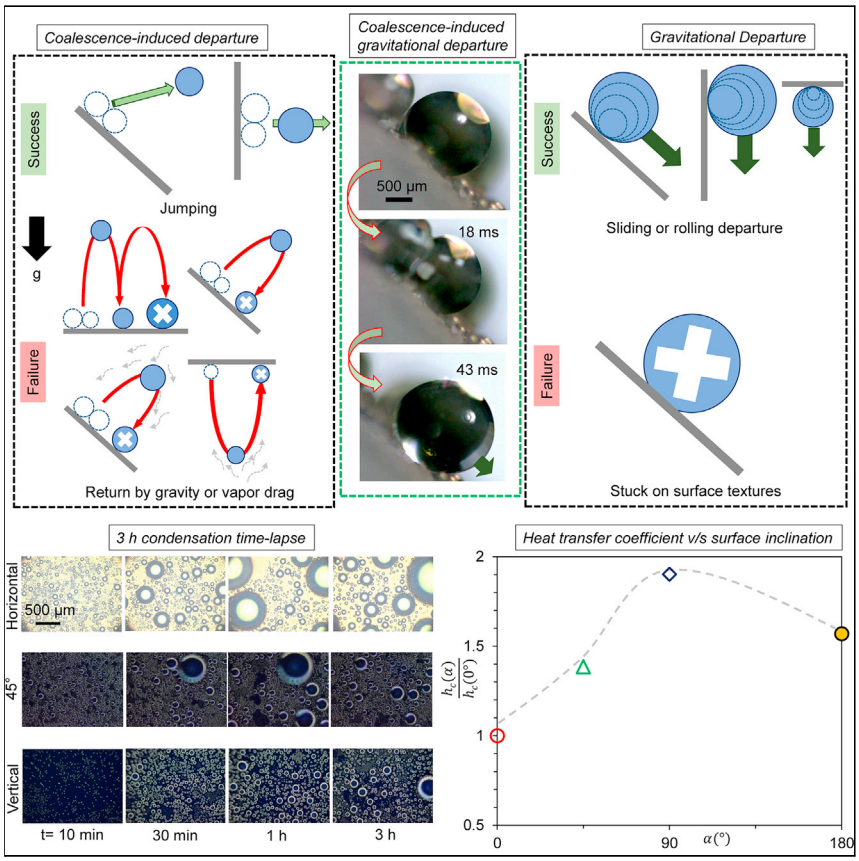

Because of its smaller condensate departure size, jumping-droplet condensation on superhydrophobic surfaces provides better heat transfer performance than does regular dropwise condensation. As the jumping mechanism is gravity independent, the effects of surface orientation on jumping-droplet condensation were previously ignored. Here, with the help of long-term condensation experiments on different surface orientations, it is shown that jumping-droplet condensers are dramatically enhanced when gravitational shedding complements the jumping. The analysis presented here can be useful in designing more efficient condensers.

Ranit Mukherjee, Austin S. Berrier, Kevin R. Murphy, Joshua R. Vieitez, Jonathan B. Boreyko

boreyko@vt.edu

HIGHLIGHTS

Jumping-droplet condensation was observed for different surface orientations

On inclined surfaces, coalescence additionally promotes gravitational removal

Phase maps characterize the various modes of gravity-assisted droplet removal

When exploiting gravity, the heat transfer of jumping-droplet condensers is doubled

Mukherjee et al., Joule 3, 1360–1376
May 15, 2019
https://doi.org/10.1016/j.joule.2019.03.004

Joule

CellPress

Article

How Surface Orientation Affects Jumping-Droplet Condensation

Ranit Mukherjee,[1] Austin S. Berrier,[1] Kevin R. Murphy,[1] Joshua R. Vieitez,[1] and Jonathan B. Boreyko[1,2,3,*]

SUMMARY

The out-of-plane jumping of coalescing droplets on superhydrophobic surfaces is capillary-inertial in nature; therefore, the effects of gravity or surface orientation are generally ignored. Here, we show that surface orientation actually has a profound effect on jumping-droplet condensation. For a horizontally oriented superhydrophobic surface, jumping droplets return to the surface and eventually become stuck. In contrast, vertical orientations can remove stuck droplets by gravitational shedding, which also serves to sweep away neighboring condensate. These differences affect the resulting droplet size distribution, which was captured using time-lapse photography and image analysis for 3 h of jumping-droplet condensation on horizontal, 45° tilted, or vertically oriented surfaces. The maximum droplet size was an order of magnitude smaller for the inclined surfaces compared to the horizontal orientation, which would enhance the theoretical heat transfer coefficient by 40% for the 45° tilt and by 100% for the vertical orientation.

INTRODUCTION

Vapor condenses on a solid substrate either as a liquid film or in the form of discrete droplets, depending upon the surface energy of the substrate.[1–3] Dropwise condensation is nearly an order of magnitude more efficient than filmwise condensation[4–6] because of the considerable thermal resistance of a continuous liquid film. The heat transfer coefficient for dropwise condensation increases monotonically as the critical size of departing droplets decreases, as this maximizes the dry surface area exposed to steam.[7,8] For conventional dropwise condensation on smooth hydrophobic surfaces, droplets are passively shed by gravity, which constrains their departure size to the capillary length (~1 mm for water).[8] Dropwise condensation is therefore well known to be highly dependent on surface orientation, where a vertical condenser minimizes the departure size and maximizes heat transfer and vice versa for horizontally oriented condensers.[9,10]

As an alternative to removing large droplets by gravity, condensing micro-droplets can spontaneously jump out of plane from nanostructured superhydrophobic surfaces upon coalescence.[11] This passive jumping mechanism serves to decrease the maximum droplet departure size of the condensate by several orders of magnitude compared to gravitationally driven dropwise condensation.[11–14] As a result, the heat transfer coefficient of jumping-droplet condensation is at least 30% higher than classical dropwise[15–17] and can be even higher when using electric fields,[18,19] tall and interconnected nanowires,[20] or overlaying hydrophilic features.[21,22]

The mechanism for out-of-plane droplet jumping is the impact of the coalescing liquid bridge against the low-adhesion substrate.[23–25] For micrometric water

Context & Scale

Condensers become more efficient when the forming dew is removed at smaller sizes. Gravity can be used to remove dew droplets at large sizes, but it was recently discovered that coalescing dew droplets can depart at micrometric sizes by jumping from a superhydrophobic condenser. As the initial jumping event is powered by surface tension instead of gravity, the effects of surface orientation have been ignored so far. Here, we show that surface orientation actually has a profound effect on the heat transfer of a jumping-droplet condenser, as inclined surfaces are capable of shedding droplets that have returned to the surface or failed to jump. By measuring the droplet size distribution at different orientations, we reveal that a gravity-assisted vertical orientation can increase the heat transfer coefficient of the condenser by 100% compared to a horizontal orientation. These findings should be useful for optimizing the efficiency of condensers in power plants or vapor chambers.

droplets, the hydrodynamics of the liquid bridge are capillary-inertial in nature as both the Bond and Ohnesorge numbers are much less than unity, indicating negligible gravitational and viscous effects.[11,12,26] Therefore, the initial out-of-plane velocity is independent of the substrate's gravitational orientation, which is why all studies to date have chosen only a single orientation to characterize jumping-droplet condensation. A theoretical study by Miljkovic et al. best summarizes the current perspective of surface orientation effects: the calculated heat transfer coefficient increases monotonically as the surface tilts from horizontal to vertical for dropwise condensation, while the heat transfer of the jumping-droplet model remains constant because of an assumption of an orientation-independent droplet distribution.[27]

While it is true that the critical departure size of a jumping droplet is orientation independent, we suggest that there are two reasons why orientation still matters. First, droplets jumping from a non-vertical surface will fall back to the surface as a result of gravity. The returned droplets can often coalesce and jump again in chain reactions[11,28,29] but will eventually grow large enough to become unable to jump. Second, jumping is suppressed if the coalescing droplets exhibit a sufficiently large mismatch in size.[30–32] In the absence of a gravitational orientation, these stuck droplets will continually grow over time, which will diminish the heat transfer.

Here, we show that the droplet size distribution and heat transfer of jumping-droplet condensation are profoundly impacted by the surface orientation of the condenser. A horizontally oriented surface was unable to shed any droplets that became stuck because of gravitational return or size mismatch, resulting in large millimetric droplets after several hours of continuous operation. For partially inclined surfaces, we found that these large, stuck droplets were instead able to roll down the surface upon coalescence-induced dislodging. This new phenomenon is a blend of capillary-inertial and gravitational effects working together synergistically. Finally, a vertically oriented surface minimized the amount of returning droplets in the first place, while retaining the supplemental gravitational removal of droplets stuck because of mismatch. A semi-empirical model was used to calculate the condensation heat flux as a function of the overall droplet size distribution for each surface orientation. Inclined orientations exhibited a 40%–100% enhancement in the theoretical heat transfer coefficient compared to the horizontal orientation due to an order-of-magnitude decrease in the maximum droplet size. These findings indicate that the performance ceiling of jumping-droplet condensers may be higher than previously expected, further motivating their potential application in power plants, HVAC (heating, ventilation, and air conditioning) systems, or thermal desalination.

RESULTS AND DISCUSSION

Surface Fabrication and Condensation Visualization

Superhydrophobic nanopillars were used for all of the condensation experiments performed here (see Experimental Procedures for details). Figure 1A shows a typical scanning electron microscope (SEM) image, where the roughly cylindrical nanopillars exhibit the following averaged values: a diameter of 69 nm, a height of 531 nm, and a center-to-center pitch of 119 nm. Deposited droplets exhibited an apparent advancing contact angle of $\theta_A \approx 160^\circ$ and an apparent receding contact angle of $\theta_R \approx 150^\circ$, as measured using the shrink-swell method on a contact angle goniometer. The advancing intrinsic contact angle on a corresponding smooth silanized silicon surface is $\theta_a \approx 113^\circ$.[14] All condensation experiments were performed by cooling the substrate down to $T_w = 1.0^\circ$C with an ambient temperature of $T_\infty \approx 20^\circ$C and a relative humidity of $RH \approx 59\%$. Time-lapse photography captured the

[1]Department of Biomedical Engineering and Mechanics, Virginia Tech, Blacksburg, VA 24061, USA

[2]Department of Mechanical Engineering, Virginia Tech, Blacksburg, VA 24061, USA

[3]Lead Contact

*Correspondence: boreyko@vt.edu

https://doi.org/10.1016/j.joule.2019.03.004

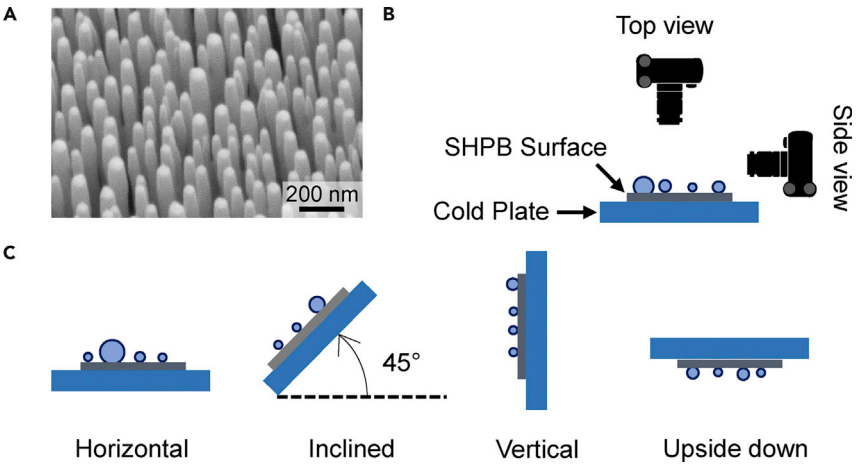

Figure 1. Experimental Setup

(A) SEM image of the silicon nanopillar arrays comprising the superhydrophobic surface used in the condensation experiments.

(B) Schematic of the experimental setup.

(C) Schematic of the condensation experiments in different surface orientations.

evolution of the droplet size distribution over 3 h of continuous condensation, as depicted in the schematic of Figure 1B. High-speed imaging was used to capture the jumping and sliding dynamics. Four different surface orientations were used: horizontal, 45°, vertical, and upside-down (Figure 1C).

The results of the time-lapse photography are shown in Figure 2 for the horizontal, 45°, and vertical orientations. Previous reports of jumping-droplet condensation have shown a near-constant droplet size distribution over time, even for a horizontal orientation.[11] However, nearly all previous visualizations of jumping droplets have only recorded a few minutes of growth for a single surface orientation.[11,13,33–36] One study by McCarthy and co-workers did report 24 h of continuous jumping-mode condensation on a vertically oriented superhydrophobic surface, but they only quantified the average droplet diameter for the first 12 min.[37] Here, the droplet size distribution was imaged over 3 h of condensation to reveal that droplets on the horizontal surface continue to grow in size over time (Figure 2A). In contrast, condensate on the 45° and vertical surfaces exhibited a near-constant size even after 3 h of continuous growth (Figures 2B and 2C).

The initial capillary-inertial jumping itself is orientation independent. To explain why the resulting droplet size distribution is still dependent on orientation, high-speed imaging was used to get a fuller picture of the range of droplet dynamics possible during growth. As expected, droplets jumping from the horizontal surface eventually returned as a result of gravity, which readily explains the increase in droplet size over time (Figure 3A). Even for inclined surfaces, droplets can still grow because of gravitational return of jumped droplets (Figure 3B), failed jumping upon coalescence as a result of size mismatch,[30–32] or vapor entrainment of jumping droplets.[18,38,39] While return by gravity is obviously not applicable to the vertical or upside-down orientations, vapor entrainment was observed even in these cases (Figure 3C). From the analysis of Miljkovic et al., for an upside-down surface orientation and a characteristic heat flux of 1 W/cm^2, the critical diameter beneath which vapor entrainment occurs is 38 μm.[18] This matches our experimental observations, where the largest jumping droplet that got entrained by the vapor flow was 33 μm for the upside-down surface. For the vertical surface, droplets as large as 70 μm returned to the surface as gravity no longer opposes vapor entrainment.

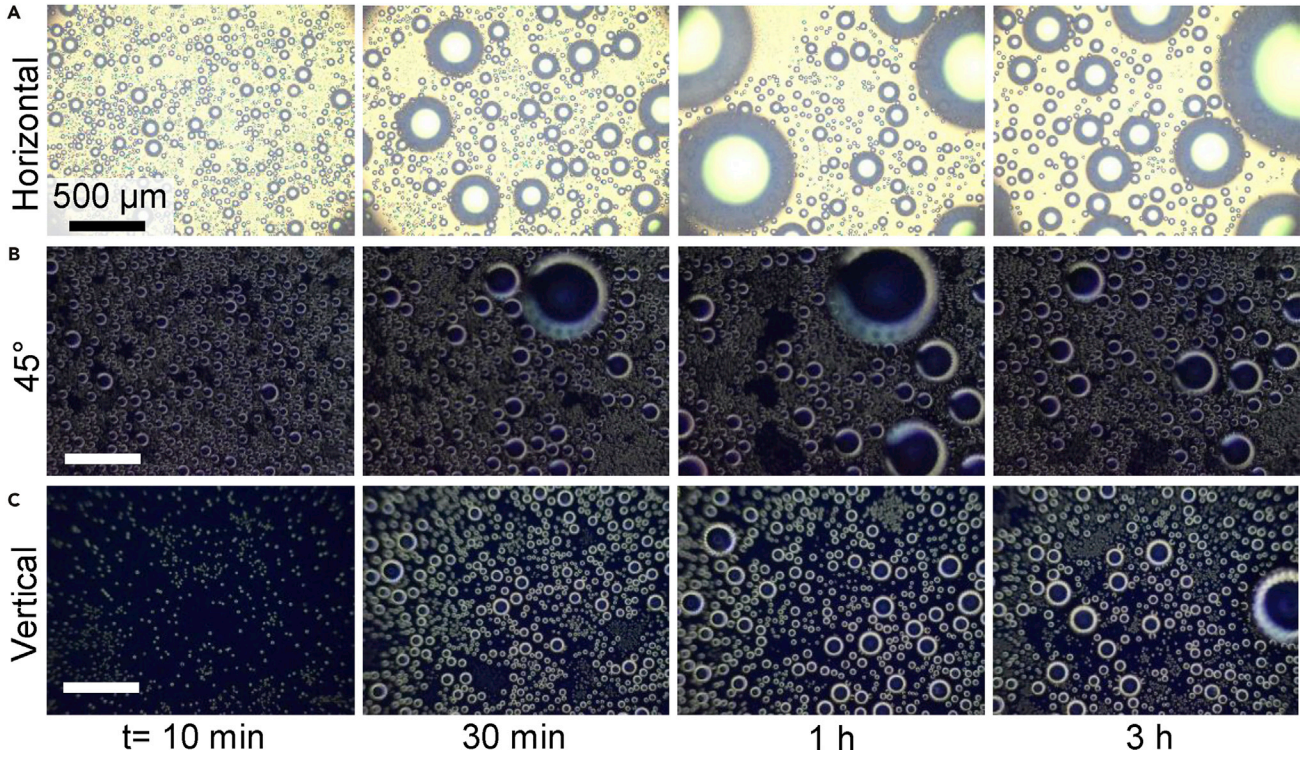

Figure 2. Time-Lapse Photography from the 3-h-Long Condensation Experiments
The surface orientations used were (A) horizontal, (B) 45° inclined, and (C) vertical.

Model of Gravity-Assisted Droplet Departure

In short, even vertical or upside-down condensers cannot fully prevent the return of jumping droplets or the failure of certain droplets to jump. However, the use of a gravitational orientation does enable the removal of droplets by sliding or falling, which would otherwise remain stuck on a horizontal surface. Regarding droplets sliding off a condenser, the critical departure size can be approximated from the analysis of Furmidge.[40] Balancing the retention force (i.e., hysteresis) of the Cassie droplet ($F_{hys|C}$) with the gravitational force (F_g):

$$\rho V_c g \sin\alpha \approx \pi a \gamma(\cos\theta_R - \cos\theta_A), \qquad \text{(Equation 1)}$$

where α is the inclination angle of the surface, ρ and γ are density and surface tension of water, respectively, $V = \frac{\pi}{3}R^3(2 - 3\cos\theta^* + \cos^3\theta^*)$ is the volume of a spherical-cap droplet exhibiting a radius of R and averaged apparent contact angle $\theta^* = \frac{1}{2}(\theta_A + \theta_R)$, and $a = R\sin\theta^*$ is the contact radius. Using $\theta_A \approx 160°$ and $\theta_R \approx 150°$, the calculated critical departure size is $2R_c \approx 915$ μm on the 45° surface and $2R_c \approx 770$ μm for the vertical surface. This is in good agreement with the experimentally observed departure size of 713 μm for a droplet sliding down the vertical surface (Figure 4A).

For the upside-down surface, droplets must detach and free fall, rather than slide. The critical size for detachment can be estimated by comparing the gravitational energy (E_g) against the work of adhesion required to detach a Cassie droplet ($E_{ad|C}$):

$$\rho V_c R g \approx \pi a^2 \gamma \phi(1 + \cos\theta_a), \qquad \text{(Equation 2)}$$

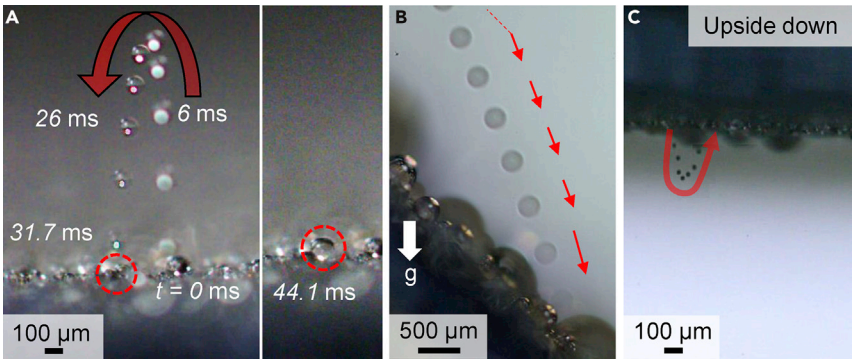

Figure 3. Images Capturing Different Droplet Removal and Return Mechanisms on the Condensing Surfaces

(A) Jumped droplets returned to a horizontal surface (first frame chronophotography) and got stuck (second frame).

(B) Chronophotography of a jumped droplet being returned to a surface at 45° inclination.

(C) A small droplet returns to an upside-down surface because of vapor entrainment. The red arrows show the droplet trajectory.

See Video S1 for visualizing droplet return on different surface orientations.

where $\phi \approx 0.295$ is the solid fraction of the pillar tops in contact with the droplet, and the averaged apparent contact angle θ^* (embedded in the expressions for V and a) is replaced by θ_A. Solving for V_c and re-expressing in terms of the droplet radius yields a critical size of $2R_c \approx 660$ μm. This gravitational removal could not be observed experimentally, as coalescence-induced detachment (which will be discussed shortly) always occurred before droplets could reach this large size.

Not all of the condensate was able to slide at sizes corresponding to Equation 1. For example, in Figure 4A, the droplet shown in red arrows continued to adhere to the vertical condenser at size $2R = 1.6$ mm even as the smaller droplet outlined in the green circle was able to slide at $2R = 713$ μm. This can be attributed to many condensate droplets not being in an idealized Cassie state but rather having a fraction of their base impaled as a Wenzel neck. This spectrum in the extent of partial impalement for jumping-droplet condensation has been directly observed by Miljkovic et al.[15] It can be understood by considering how a droplet originally nucleates and inflates within the nanostructure. A liquid embryo is initially of size ~1–10 nm,[41] such that it can nucleate somewhere inside of a unit cell of roughness.[42] In such cases, the water initially fills a unit cell(s) in a Wenzel state but can subsequently inflate into a Cassie state beyond this impaled neck.[43] This energetic comparison for inflating in the Cassie versus Wenzel states can be simply expressed as[42]

$$E^* = -\frac{1}{r\cos\theta_a}, \qquad \text{(Equation 3)}$$

where θ_a is the intrinsic advancing contact angle on a smooth silanized surface, and r is the surface roughness. A nucleated droplet prefers to inflate into the Cassie state if $E^*<1$; here, we get $E^* = 0.28$ for our surface parameters of $\theta_a = 113°$ and $r = 9.12$. However, even when $E^* < 1$ and the outer perimeter of the droplet is in the Cassie state, the central portion of the droplet still exhibits a Wenzel state from where it initially nucleated. This explains why some of our droplets approximate a pure Cassie state, where Equations 1 and 2 are valid, while others exhibit a much higher degree of pinning where new equations now need to be formulated.

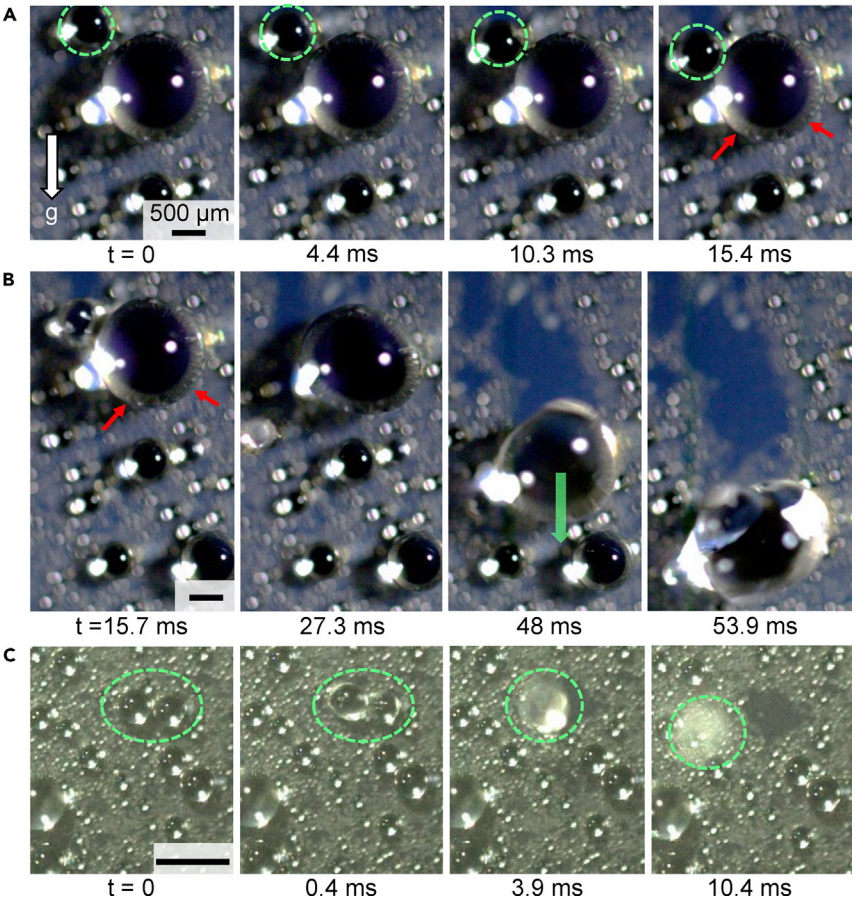

Figure 4. Gravitational Sliding of Droplets on a Vertically Oriented Surface

(A) The droplet marked in the green circle started sliding as it was near the critical departure size for Cassie droplets on the vertically oriented condenser. Even though the droplet marked in red arrows was much bigger than the sliding droplet, it was stuck because of impalement on the surface structures.

(B) The bigger droplet (red arrows) started sliding after coalescing with the smaller droplet (green circle).

(C) For an upside-down surface orientation, droplets virtually always fall or jump from the surface upon coalescence (green circle).

For Wenzel droplets on a highly roughened and superhydrophobic surface, the contact angle hysteresis approaches its maximal value: $\theta_A \rightarrow 180^\circ$ and $\theta_R \rightarrow 0^\circ$.[44] This Wenzel state therefore modifies the hysteresis term in Equation 1 to $(\cos\theta_R - \cos\theta_A) \approx 2$. Comparing gravity ($F_g$) to the Wenzel hysteresis force ($F_{hys|W}$) yields the modified Furmidge equation:

$$\rho V_c g \sin\alpha \approx 2\pi a\gamma. \qquad \text{(Equation 4)}$$

This results in a critical diameter of $2R_c \approx 4.2$ mm for vertical orientation, nearly an order of magnitude larger than that for Cassie droplets. Similarly, for the upside-down orientation, the work of adhesion term must be modified for a droplet in the partial Wenzel state. For a Wenzel neck of radius r_p, beyond which the droplet is in the Cassie state, the competition between gravity (E_g) and work of adhesion ($E_{ad|W}$) now becomes

$$\rho V_c R g \approx 2\pi r_p^2\gamma(1-\phi) + \pi a^2\gamma(1+\cos\theta_a)\phi, \qquad \text{(Equation 5)}$$

where the first term on the right-hand side represents the energy required to rip the droplet from its neck, and the second term is the energy for detaching the liquid-solid interface from the pillar tops. The value of r_p for a given surface structure can be estimated by the three-stage energetic growth model developed by Mulroe et al.[14] (see corresponding Section 1 and Figure S1 of the Supplemental Information). Using 119, 531, and 69 nm as the average geometrical values of pitch, height, and diameters of our nanopillars, respectively, we obtain $r_p \approx 0.30\,\mu m$. Using this value of r_p, we get $2R_c \approx 1.8$ mm, which is three times larger than the critical fall-off size for Cassie droplets.

Besides gravitational removal for Cassie droplets or Wenzel droplets, we discovered a third mechanism for gravitationally driven droplet removal. In Figure 5A, it was observed that the surface energy released upon coalescence was sufficient to detach Wenzel droplets from their impaled necks. In other words, for larger droplets, coalescence can no longer produce jumping but can be sufficient for detaching from Wenzel necks. Besides detachment, another hypothetical possibility is for the impaled necks to dewet (i.e., recede) out of the cavities. However, it is now well known that the impaled Wenzel state is almost always irreversible,[45–47] as the energy barrier for pinch-off is lower than that for dewetting.[48] A final scenario of coalescence actually increasing the extent of droplet impalement was ruled out from energetic[45] and physical criteria[3] shown in Section 2 of the Supplemental Information.

The schematic shown in Figure 5B represents the model used to rationalize this coalescence-induced detachment. When two (or more) droplets coalesce with each other, they release excess surface energy.[11] Assuming a spherical cap geometry for two similar-sized droplets in a partial Wenzel state, from simple geometric relations we can write the excess surface energy due to coalescence as[49]

$$\Delta E_s = \pi\gamma\left[4R^2(\cos\theta_{app}-1) - 2^{\frac{4}{3}}R^2\left[(2+\cos\theta_{app})(\cos\theta_{app}-1)^2\right]^{\frac{2}{3}}\right], \quad \text{(Equation 6)}$$

where R is the radius of the droplets before coalescence, and θ_{app} is the apparent contact angle of each droplet. Using Figure 5B as an example, $R \approx 867\,\mu m$, while $\theta_{app} = \theta_A = 160^\circ$ from the aforementioned goniometric measurements of deposited droplets. While it is true that the deposited droplets were in a Cassie state while the droplets here exhibited a Wenzel neck, the outermost perimeter of these pinned droplets is in the Cassie state, which governs the angle. Plugging these values into Equation 6 yields $\Delta E_s \approx 10^{-6}$ J. This excess energy must overcome the work of adhesion required for detachment from the impaled necks. Before coalescence, each droplet is pinned by a Wenzel neck of cross-sectional area $A_p = \pi r_p^2$. The work of adhesion to detach two droplets from their Wenzel necks, while the merged droplet still rests atop the pillars, is given by

$$E_{ad|N} \approx 4\pi r_p^2\gamma(1-\phi). \quad \text{(Equation 7)}$$

If the ratio of $\Delta E_s/E_{ad|N} \gg 1$, then droplets will detach from their pinned necks upon coalescence. For our surface, we found that $E_{ad|N} \approx 10^{-14}$ J, which results in $\Delta E_s/E_{ad|N} \approx 10^8 \gg 1$ for a droplet radius of $R = 867\,\mu m$. When the merged droplet exceeds the critical diameter for sliding in the Cassie state (Equation 1), departure occurs immediately upon coalescence-induced detachment from the Wenzel necks. For example, the aforementioned 1.6 mm droplet stuck to the vertical surface (Figure 4A) was able to shed immediately after merging with a smaller droplet (Figure 4B), as a critical diameter of only 770 μm is required once in the Cassie state (Equation 1). For the example on the 45° surface (Figure 5A), the droplet was $2R \approx 2$ mm after coalescence, which similarly exceeds the critical diameter of 915 μm.

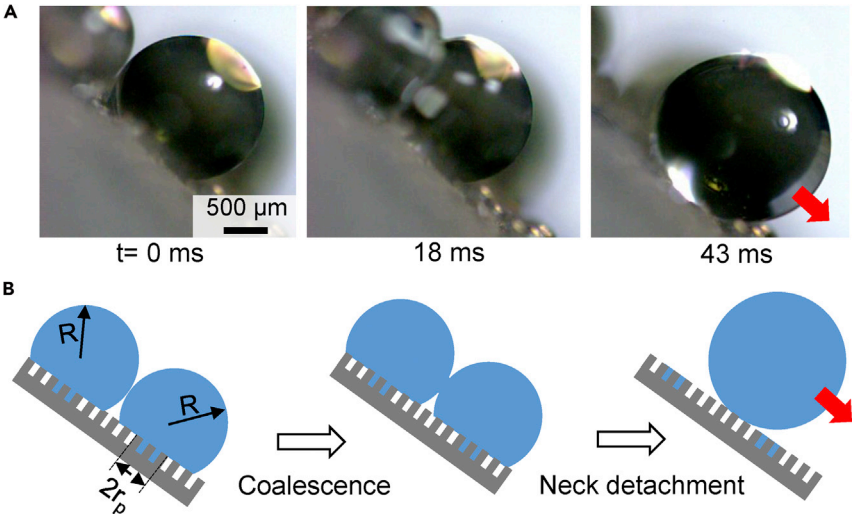

Figure 5. Coalescence-Induced Neck Detachment and Subsequent Gravitational Sliding

(A) Side-view imaging of gravitational shedding facilitated by coalescence on a 45° inclined surface. Initially, the two droplets are pinned on the surface despite being millimetric in size. As the two droplets coalesce together, the released surface energy is used to detach the merged droplet from the impaled Wenzel necks, enabling sliding in a Cassie state. See also Video S2.

(B) Schematic of the coalescence-induced gravitational droplet departure mechanism.

Coalescence can also overcome the work of adhesion required to detach impaled droplets from an upside-down condenser, at which point gravity induces droplet falling (Figure 4C). Comparing the same surface energy released upon coalescence to the work of adhesion for droplet detachment, we get the following equation:

$$\pi\gamma\left[4R_c^2(\cos\theta_{app}-1)-2^{\frac{4}{3}}R_c^2\left[(2+\cos\theta_{app})(\cos\theta_{app}-1)^2\right]^{\frac{2}{3}}\right]\approx 4\pi r_p^2\gamma(1-\phi)+2\pi a_c^2\phi\gamma(1+\cos\theta_a), \quad \text{(Equation 8)}$$

where $a_c = R_c\sin\theta_A$ is the contact radius of each droplet before coalescence. This equation can be solved for the critical value of R_c.

To our knowledge, gravitational shedding enabled by coalescence-induced droplet detachment has not been previously reported. Past studies have instead focused on the ability of coalescence to trigger out-of-plane jumping[11,24,25] or in-plane sweeping[36,50] for micrometric droplets where gravity was not playing a role. Other works have characterized the chain reactions triggered by jumping droplets returning to the surface for subsequent coalescence-induced jumping events.[11,28,51] Finally, it has been shown that coalescence can trigger dewetting[52,53] or neck detachment[12,49] to switch the merged droplet to the Cassie state, but only for microscopic droplets on a horizontal substrate. Instead of only using coalescence to eject microscopic condensate, our findings indicate that coalescence can work in tandem with gravity to remove mid-sized droplets that could not be removed by surface tension or gravity in isolation.

In Figure 6, we have constructed phase maps that graph the critical departure radius for each possible mode of droplet detachment and departure. The critical radii were non-dimensionalized by the capillary length of water: $l_c = \sqrt{\gamma/\rho g} \approx 2.7$ mm. The red region in the bottom of each phase map represents nanoscale condensate that has

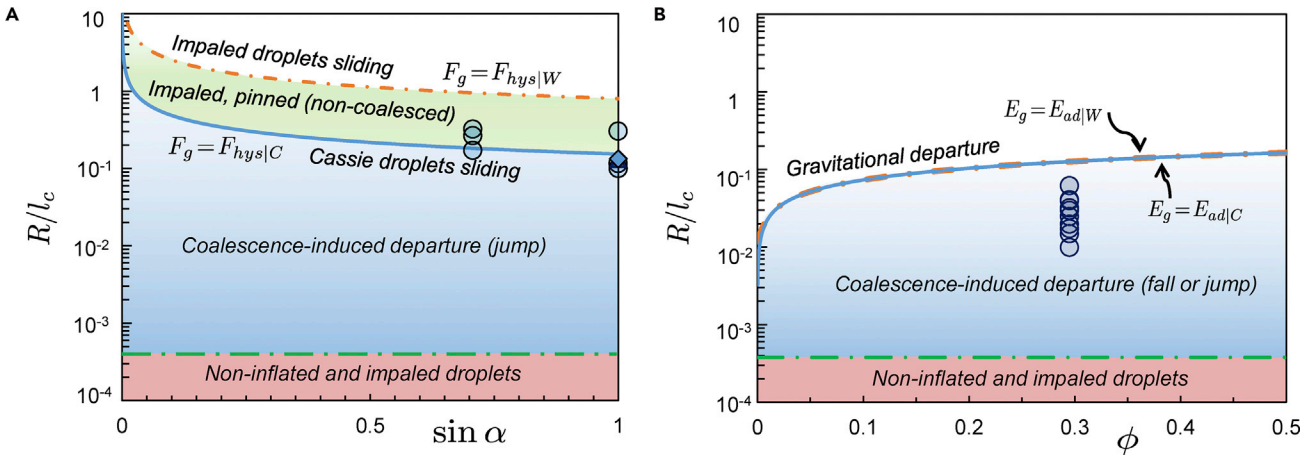

Figure 6. Semi-log Phase Maps Showing the Different Regimes of Gravity-Assisted Removal of Condensate from Superhydrophobic Surfaces

Both Cassie droplets and impaled droplets with Wenzel necks are considered.

(A) For inclined orientations, the non-dimensionalized critical droplet radius (R/l_c) depends on the inclination angle (α). The green dashed line represents the minimum size for the coalescence-induced jumping of an inflated droplet. The blue circles are all experimental observations of droplets shedding by gravity after coalescence-induced neck detachment. The blue diamond is the only experimental case of an isolated Cassie droplet sliding by gravity upon reaching the critical size.

(B) For an upside-down surface, R/l_c now depends primarily upon the solid fraction governing the work of adhesion. Experimental data points for the coalescence-induced droplet detachment and falling are shown by the blue circles.

not yet been able to inflate to large apparent contact angles. Prior to inflation, such droplets are not prone to removal from either coalescence or gravitational mechanisms. The green dotted line in each map represents the critical size above which coalescence-induced jumping is now possible, $R/l_c \sim 10^{-4}$, because of the droplets now being inflated.[14] As already discussed, as a result of various factors including entrainment or size mismatch, some droplets will remain stuck to the surface even in the blue regions above the green dotted lines. The remaining aspects of the phase maps differ depending on whether the surface is inclined or upside-down, which will now be discussed in turn.

For inclined surfaces (Figure 6A), droplets stuck on the surface can at least detach from their Wenzel necks upon coalescence in the blue region above the green line. This is because the two necessary conditions are both satisfied: the droplets are inflated to large angles (i.e., above green line) and the surface energy gained upon coalescence can overcome the work of adhesion required to detach from the necks, as $\Delta E_s/E_{ad|N} > 1$ for micro-scale droplets (Equations 6 and 7). The detachment of impaled droplets in the blue region of the phase map could not be observed, as the Wenzel necks within the nanostructure are too small to be optically resolved while the droplets themselves still remain pinned on the surface. The solid blue line represents the critical droplet size where Cassie droplets can slide off the surface by gravity (Equation 1). The blue diamond symbol corresponds to the critical size of an isolated Cassie droplet sliding down the surface, as measured in Figure 4A, in excellent agreement with the blue theory line. The green region above this blue line represents droplets still in the impaled state, where as soon as they coalesce to detach into the Cassie state they can therefore immediately slide down the surface. Experimental measurements of this coalescence-induced detachment and sliding are shown as blue circles. Finally, for any unlucky impaled droplets that never coalesced with similar-sized neighboring condensate, gravitational sliding within the impaled state is estimated by the orange dotted

line (Equation 4). No experimental observations of impaled droplet sliding were observed, as coalescence always occurred before growing to a size commensurate with the orange line.

An analogous phase map can be drawn for the upside-down orientation (Figure 6B). Now, gravity no longer facilitates droplet sliding along the surface but rather causes droplets to fall from the surface once their work of adhesion is overcome. This is why the upside-down phase map now plots the droplet size against the solid fraction of the surface (ϕ), as the work of adhesion is a function of the droplets' contact area with the pillar tops. For condensate impaled with Wenzel necks, recall the critical size above which the energy gained from two-droplet coalescence overcomes the work of adhesion, which is given by Equation 8. This results in $R/l_c \sim 10^{-5}$, an order of magnitude smaller than the size required for the droplets to inflate and coalesce in the first place (green line). Therefore, the blue region above the green line satisfies the dual criteria for impaled droplets to both be inflated and result in coalescence-induced detachment and falling from the surface. Blue circles depict the experimentally measured droplet sizes where coalescence-induced detachment and subsequent gravitational falling occurred. Comparing ΔE_s to the work of adhesion for droplets able to initialize in the Cassie state ($E_{ad|C}$), we found that droplets of any size will detach upon coalescence, which could not be shown directly in the phase map. This is expected to be the minority case, however, as most condensate originate with Wenzel necks. For hypothetical droplets that do not coalesce, gravity eventually overcomes the work of adhesion at much larger sizes. This is shown for Cassie droplets (Equation 2) or droplets with Wenzel necks (Equation 5) with the blue and orange lines, respectively. While the critical size for gravity-induced detachment was lower for Cassie droplets compared to Wenzel, this distinction was so small that the phase lines virtually overlap. This is because the pillar top adhesion dominates over that of the small Wenzel neck for droplets of this size.

Heat Transfer Analysis

The demonstrated orientation dependence of gravity-induced droplet departure rationalizes the contrasting droplet size distributions shown in Figure 2. These disparate droplet size distributions are quantified in Figure 7 using image analysis over the full 3 h of growth. The average droplet size increased continuously to about $D_{avg} \approx 100$ μm after 3 h of growth on the horizontal surface. In contrast, a smaller plateau value of $D_{avg} \approx 30$ μm was reached on both the 45° inclined and vertical surfaces (Figure 7A).

The maximum droplet size was $D_{max} \approx 1.4$ mm and climbing for the horizontal surface, nearly an order of magnitude larger than the stable value of $D_{max} \approx 160$ μm on the vertical surface (Figure 7B). The maximum droplet diameter measured here for the vertical orientation is smaller than the sliding diameter shown in Figure 4A. This is because jumping droplets do not tend to return to the surface for a vertical orientation, such that droplets as large as that shown in Figure 4A are extremely rare and not visible in the field of view used for the Figure 7 measurements. In Figure 7B, the maximum droplet diameter on the 45° inclined surface is slightly larger than the horizontal orientation for the first hour. This can be explained by the stochastic nature of droplet nucleation (particularly for small fields of view) and also by the fact that the gravitational removal offered by the inclined surface is not enabled until droplets have time to grow to larger sizes.

The projected surface coverage of dropwise condensation plateaus to a self-similar value, typically about $\epsilon^2 \approx 0.6$.[54,55] Our horizontal surface exhibited a

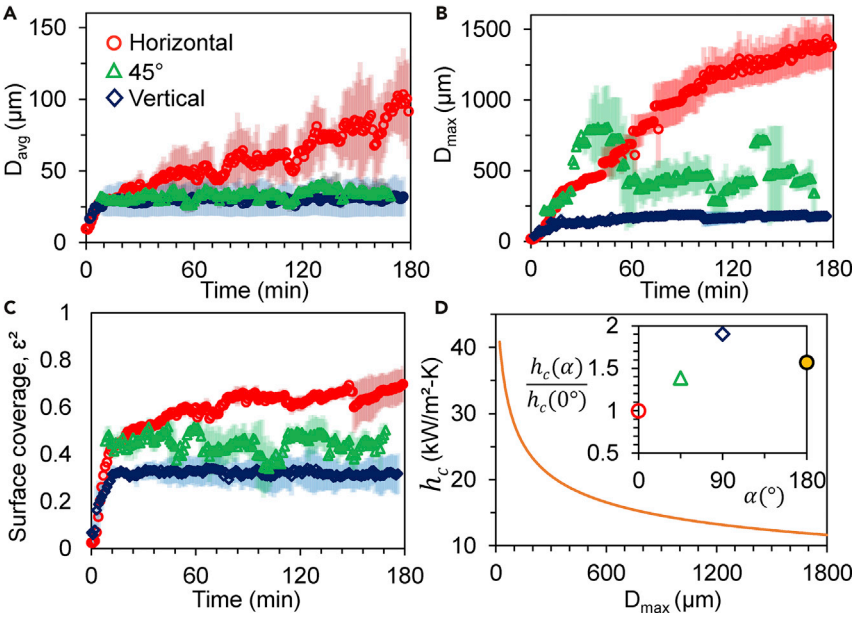

Figure 7. Summary of Orientation-Dependent Droplet Size Distributions and Their Effects on Heat Transfer

(A–C) Variation of the (A) average droplet diameter, (B) maximum droplet diameter, and (C) fraction of the condensing surface covered by the droplets with time for different surface orientations. Error bars represent one standard deviation over three trials for the horizontal and 45° orientations and over two trials for the vertical orientation.

(D) Exponential decay of the theoretical steady-state condensation heat transfer coefficient (h_c) with increasing maximum droplet diameter (D_{max}) on the surface with $\hat{\alpha} = 0.35$ and $\Delta T = 5$ K. Inset: heat transfer coefficients at different surface inclinations with respect to that for a horizontal orientation.

self-similar value of $\epsilon^2 \approx 0.7$, significantly more than the 45° inclined ($\epsilon^2 \approx 0.45$) or vertical ($\epsilon^2 \approx 0.3$) surfaces (Figure 7C). These findings can all be explained by the inability of the horizontal surface to shed returning jumping droplets (or droplets that failed to jump because of size mismatch), while the inclined surfaces could shed such droplets gravitationally by the mechanisms summarized in Figure 6. Given that Wenzel necks remain impaled within the surface, even after droplet detachment and departure, flooding could be a concern as new droplets (and necks) form over time. Flooding was not observed here, however, as evidenced by the steady-state surface coverage. We attribute this to the lower nucleation energy barrier of the wet unit cells (i.e., necks) causing subsequent droplets to inflate in the same regions.

Using the measured values of D_{max}, the condensation heat transfer coefficient can be estimated using the model established by Le Fevre and Rose[7] with modifications accounting for the superhydrophobic structured surfaces.[15,56] The heat transferred across a single droplet of radius r is expressed as

$$q_d(r) = \frac{\pi r^2 \left(\Delta T - \frac{2T_{sat}\gamma}{rh_{fg}\rho}\right)}{\frac{1}{2h_i(1-\cos\theta)} + \frac{r\theta}{4k_w \sin\theta} + \frac{1}{k_c \sin^2\theta}\left[\frac{k_p\phi}{\delta_c k_p + hk_c} + \frac{k_w(1-\phi)}{\delta_c k_w + hk_c}\right]^{-1}}, \quad \text{(Equation 9)}$$

where ΔT is the degree of subcooling; T_{sat} is the saturation temperature of the water vapor; h_{fg} is the latent heat of vaporization; h_i is the interfacial condensation heat

transfer coefficient; δ_c is the thickness of the conformal hydrophobic coating; h is the height of the nanopillars; and k_w, k_p, and k_c are the thermal conductivities of water, silicon, and the hydrophobic coating, respectively. The interfacial heat transfer coefficient is itself given by

$$h_i = \frac{2\widehat{\alpha}}{2-\widehat{\alpha}} \frac{1}{\sqrt{2\pi R_g T_{sat}}} \frac{h_{fg}^2}{\nu_g T_{sat}}, \qquad \text{(Equation 10)}$$

where R_g is the specific gas constant, ν_g is the water vapor specific volume at T_{sat}, and $\widehat{\alpha}$ is the condensation coefficient ranging from 0 to 1, where $\widehat{\alpha} = 1$ signifies the complete condensation of all vapor molecules impinging on the liquid surface. As the heat transfer coefficient does not vary widely with $\widehat{\alpha}$, we have used a representative value of $\widehat{\alpha} = 0.35$ in our model.[57] This results in a value of $h_i = 0.1$ MW/m^2•K, close to the value reported by Kim and Kim.[56] The total condensation heat transfer coefficient, h_c, can then be found by integrating $q_d(r)$ across the entire droplet size distribution

$$h_c = \frac{q''}{\Delta T} = \frac{1}{\Delta T}\left[\int_{r_{min}}^{r_{col}} q_d(r)n(r)\mathrm{d}r + \int_{r_{col}}^{r_{max}} q_d(r)N(r)\mathrm{d}r\right], \qquad \text{(Equation 11)}$$

where $n(r)$ and $N(r)$ are the size distributions below and above the typical length scale, respectively, where coalescence occurs. See Section 3 of the Supplemental Information for the expressions of $n(r)$ and $N(r)$ for a condensing superhydrophobic surface, which has been previously reported.[27] For the heat transfer modeling, we have neglected the effect of sweeping as there was not a significant change in the value of heat transfer coefficient and also, qualitatively, the variation of h_c with maximum droplet radius remained the same (see Figure S2 in the Supplemental Information).

For the simplicity of the model, we have assumed a static contact angle, $\theta = \theta_A = 160^\circ$, for the droplets. Although this induces an error in the total heat-flux measurement for droplets below 8 μm,[27] for our purpose of providing a qualitative comparison of heat transfer performance in different surface orientations, this error in the model can be neglected. Using fixed values of T_{sat} = 287.15 K, ΔT = 5 K, hydrophobic coating thickness δ_c = 1 nm, thermal conductivity k_c = 0.2 W/m-K, pillar height h = 531 nm, and conductivity k_p = 150 W/m-K, we can see how h_c varies with changes in the maximum droplet diameter, $D_{max} = 2r_{max}$. Figure 7D shows that with increased maximum droplet diameter on the surface, condensation heat transfer coefficient decreases exponentially. Le Fevre and Rose observed a similar trend for their model of dropwise condensation on a smooth hydrophobic surface.[7]

In the inset of Figure 7D, theoretical values of h_c are shown corresponding to experimentally measured values of D_{max} for the different surface orientations. For the horizontal surface, the maximal droplet size is always increasing with time, so we used the final measured value of $D_{max} \approx 1.3$ mm at the 3 h mark. For the 45° and vertical surface inclinations, the value of D_{max} plateaus because of gravitational shedding. For $\alpha = 45^\circ$, the plateau value of D_{max} oscillated in time, which we attribute to the small field of view combined with chain reactions of one jumping and/or sliding droplet sweeping away many others. Thus, we averaged these oscillatory plateau values together to obtain $D_{max} \approx 498$ μm. For the vertical surface, a constant plateau value of $D_{max} \approx 167$ μm was observed after the initial transient. A 3-h experiment was not conducted for the upside-down orientation, as this would have resulted in many droplets obscuring the lens. However, from the "bottom-up" imaging of an

upside-down condenser, we observed the largest possible droplet size prior to coalescence-induced detachment and falling. Discounting local areas where scratches or defects were visibly present, we observed that the largest departing droplets were approximately $D_{max} \approx 334$ μm after at least 2 h of continuous condensation.

Because of these orientation-dependent disparities in D_{max}, the condensation heat transfer was enhanced by approximately 40% for $\alpha = 45°$ and by 100% for $\alpha = 90°$ compared to the horizontal condenser. The upside-down surface exhibited a higher h_c than both the horizontal and 45° orientation, but lower than the vertical orientation. This can be rationalized by the fact that both the upside-down and vertical orientations have a lower frequency of returning droplets compared to the 45° and horizontal surfaces. In turn, the vertical surface being slightly better than the upside-down can be explained by the beneficial sweeping effect that is exclusive to droplets sliding down an incline.

The heat transfer model used to find the theoretical heat transfer coefficient presumes that the non-condensable gases (NCGs) have been removed from the system. When NCGs are present, as in the case of our experiments, they act as a diffusive barrier to the water vapor.[58–60] This slows the growth rate of condensate and decreases the heat transfer coefficient but is not expected to affect the orientation-dependent droplet dynamics captured here, which govern the maximum droplet sizes. The droplet size distribution is also a function of the coalescence length scale, which is related to the nucleation density and depends on both the supersaturation and the concentration of NCGs. Here, we chose a value of $r_{col} = 1$ μm that is representative of our surface and experimental conditions (see Section 3 in the Supplemental Information). In the absence of NCGs, the actual subcooling (within the water vapor layer) can increase for the same supersaturation, which may result in surface flooding.[61] It has recently been shown that this issue can be mitigated by using tall and dense nanowires that promote nucleation atop the surface.[20]

These trends are qualitatively similar to those reported by Koch et al. for dropwise condensation on a smooth surface, where the vertical orientation performed the best and the flat surface performed the worst.[10] However, extending this concept of orientation dependence to jumping-droplet condensation for the first time results in some interesting new insights. For example, recent experimental measurements of jumping-droplet heat transfer coefficients have found 30%[16] and 60%[21] enhancements compared to dropwise condensation on a smooth surface. The superior performance of the latter case was exclusively attributed to the addition of hydrophilic bumps to increase the nucleation density, but we suggest it could additionally be due to its vertical orientation compared to the use of a horizontal tube in the former case. Indeed, the report using a horizontal tube did very briefly mention an observation of larger droplets at the bottom of the tube compared to the sides,[16] which is better understood in light of our present work. Follow-up studies should experimentally measure h_c for a superhydrophobic surface with different surface orientations and also pay more attention to a possible time dependence for h_c, especially for the horizontal case. Finally, the measured contact angle hysteresis for Cassie droplets (≈10°) is relatively high on our present surface compared to other superhydrophobic surfaces; it is probable that the heat transfer of the vertical orientation could be even further enhanced using more advanced surface structures.

In conclusion, we have shown that the dynamics of jumping-droplet condensation are heavily affected by gravity and surface orientation. While larger droplets become stuck on a horizontal superhydrophobic condenser, they are capable of sliding down an inclined surface or detaching from an upside-down surface. We also identified that coalescence can serve to detach larger droplets from their pinned Wenzel necks, which substantially reduces the critical size required for gravitational sliding. These orientation-dependent shedding dynamics directly affect the resulting droplet size distribution of growing condensation, which in turn affects the heat transfer coefficient. Compared to the baseline case of a flat condenser, a jumping-droplet surface inclined by 45° or 90° should exhibit an increase in heat transfer of 40% and 100%, respectively. These findings should have profound implications regarding our understanding of jumping-droplet condensation heat transfer; for example, a vertical wall should perform better than horizontal tubes. Given that jumping-droplet condensation already exhibits a higher heat transfer coefficient than any other form of condensation, the ability to increase performance even further with an optimal surface orientation should motivate future implementation in power plants and HVAC systems.

EXPERIMENTAL PROCEDURES

Superhydrophobic Surface Preparation

The nanopillared superhydrophobic surfaces were made in the cleanroom of the Center for Nanophase Materials Sciences at the Oak Ridge National Laboratory. The silicon nanopillars were fabricated non-lithographically by dry etching into a thermally dewet platinum film that served as the etch mask. For more details on the fabrication process, please refer to the previous reports by Boreyko and co-workers[14,62] The nanopillars have a height of $h = 531 \pm 6$ nm, diameter of $d = 69 \pm 8$ nm, and center-to-center pitch of $p = 119 \pm 40$ nm. The nanopillars were conformally coated with a hydrophobic monolayer by the vapor-phase deposition of trichloro(1H, 1H, 2H, 2H–perfluorooctyl)silane (Sigma-Aldrich). The silicon sample and an open vial of the liquid silane were held within a container on a hot plate set to 70°C for several hours. Surface characterization was done on a contact angle goniometer (ramé-hart) using the droplet shrink-swell method. The apparent advancing and receding contact angles for water on the superhydrophobic surface were measured to be $\theta_A = 161° \pm 1°$ and $\theta_R = 151° \pm 4°$, respectively.

Condensation Experiments Setup

The condensation experiments were performed either in the ambient or in a customized humidity chamber (ramé-hart) with the nanostructured surface thermally bonded to a Peltier cold stage (ramé-hart) with the help of a thermal paste (Aavid Thermalloy). The temperature of the cold stage was set at $T_w = 1.0$°C with an ambient air temperature of $T_\infty = 20 \pm 4$°C and a relative humidity of $RH = 59\% \pm 2\%$. This corresponds to an average supersaturation of $S = 2.1 \pm 0.4$, where $S = P_v/P_{sat}(T_w)$ is the ratio of the partial vapor pressure of the ambient air and the saturation pressure of water vapor at the substrate temperature. Condensation visibly appeared in the camera images about 30 s after reaching $T_w = 1.0$°C, which corresponds to our definition of time zero for the 3-h growth experiments.

For the horizontal orientation, a high-speed camera (Phantom v711, Vision Research) was used along with a function generator (Agilent, 10 MHz) for capturing top-down images of the condensing surface at 10-s intervals for 3 h. For the 45° inclined and vertical orientation experiments, a Nikon D5300 camera attached to an Infiniprobe TS-160, two extension tubes, and a ring light (Polaroid) were used. The high-speed

videos of the dynamics of the condensing droplets on horizontal, 45° inclined, vertical, and upside-down surface orientations were captured from three different angles, e.g., top-down, bottom-up, and side view using the high-speed camera (Phantom v711).

Image Analysis

Image analysis techniques were used to calculate the number of droplets within the field of view and individual droplet diameter from the time-lapse images of experiments. From these two sets of data, average and maximum droplet diameter over 3-h condensation and surface coverage by the condensates were calculated. Even though images were taken at every 10 s during the actual experiments, to save time, images at 1-min intervals were used for all of the analyses. Images on the horizontal surface orientation were analyzed with the help of an image processing software (ImageJ). All images were converted to binary images before a droplet edge-detection algorithm was applied. For the 45° inclined and vertical orientation images, custom Java codes were used for the image analysis.

SUPPLEMENTAL INFORMATION

Supplemental Information can be found online at https://doi.org/10.1016/j.joule.2019.03.004.

ACKNOWLEDGMENTS

This work is supported by Award No. 2018-67013-28063 from the USDA National Institute of Food and Agriculture (NIFA).

AUTHOR CONTRIBUTIONS

J.B.B. conceived the research. A.S.B., J.R.V., and R.M. carried out the experiments. K.R.M. and R.M. analyzed the images. R.M. and J.B.B. interpreted the results and developed the theoretical modeling. R.M. and J.B.B. wrote the manuscript. All authors proofread, added comments, and approved the manuscript.

DECLARATION OF INTERESTS

The authors declare no competing interests.

Received: December 21, 2018
Revised: February 15, 2019
Accepted: March 8, 2019
Published: April 3, 2019

REFERENCES

1. Rose, J.W. (1988). Some aspects of condensation heat transfer theory. Int. Commun. Heat Mass Transfer *15*, 449–473.

2. Rose, J.W. (2002). Dropwise condensation theory and experiment: a review. Proc. Inst. Mech. Eng. Part A: J Power Energy *216*, 115–128.

3. Oh, J., Zhang, R., Shetty, P.P., Krogstad, J.A., Braun, P.V., and Miljkovic, N. (2018). Thin film condensation on nanostructured surfaces. Adv. Funct. Mater. *28*, 1–10.

4. Schmidt, E., Schurig, W., and Sellschopp, W. (1930). Versuche uber die Kondensation von Wasserdampf in Film- and Tropfenform. Tech. Mech. Thermodyn. *1*, 53–63.

5. Beysens, D., and Knobler, C.M. (1986). Growth of breath figures. Phys. Rev. Lett. *57*, 1433–1436.

6. Fritter, D., Knobler, C.M., and Beysens, D.A. (1991). Experiments and simulation of the growth of droplets on a surface (breath figures). Phys. Rev. A *43*, 2858–2869.

7. Le Fevre, E.J., and Rose, J.W. (1966). A theory of heat transfer by dropwise condensation. In Proceedings of the Third International HEAT Transfer Conference (Chicago, IL), pp. 362–375.

8. Tanasawa, I. (1974). Critical size of departing drops. In Proceedings of the Fifth International HEAT Transfer Conference, Volume 7 (Tokyo, Japan), p. 188.

9. Citakoglu, E., and Rose, J.W. (1969). Dropwise condensation—the effect of surface inclination. Int. J. Heat Mass Transf. *12*, 645–651.

10. Koch, G., Zhang, D.C., and Leipertz, A. (1997). Condensation of steam on the surface of hard coated copper discs. Heat Mass Transf. *32*, 149–156.

11. Boreyko, J.B., and Chen, C.H. (2009). Self-propelled dropwise condensate on

superhydrophobic surfaces. Phys. Rev. Lett. *103*, 184501.

12. Cha, H., Xu, C., Sotelo, J., Chun, J.M., Yokoyama, Y., Enright, R., and Miljkovic, N. (2016). Coalescence-induced nanodroplet jumping. Phys. Rev. Fluids *1*, 064102.

13. Mouterde, T., Lehoucq, G., Xavier, S., Checco, A., Black, C.T., Rahman, A., Midavaine, T., Clanet, C., and Quéré, D. (2017). Antifogging abilities of model nanotextures. Nat. Mater. *16*, 658–663.

14. Mulroe, M.D., Srijanto, B.R., Ahmadi, S.F., Collier, C.P., and Boreyko, J.B. (2017). Tuning superhydrophobic nanostructures to enhance jumping-droplet condensation. ACS Nano *11*, 8499–8510.

15. Miljkovic, N., Enright, R., and Wang, E.N. (2012). Effect of droplet morphology on growth dynamics and heat transfer during condensation on superhydrophobic nanostructured surfaces. ACS Nano *6*, 1776–1785.

16. Miljkovic, N., Enright, R., Nam, Y., Lopez, K., Dou, N., Sack, J., and Wang, E.N. (2013). Jumping-droplet-enhanced condensation on scalable superhydrophobic nanostructured surfaces. Nano Lett. *13*, 179–187.

17. Zhu, J., Luo, Y., Tian, J., Li, J., and Gao, X. (2015). Clustered ribbed-nanoneedle structured copper surfaces with high-efficiency dropwise condensation heat transfer performance. ACS Appl. Mater. Interfaces *7*, 10660–10665.

18. Miljkovic, N., Preston, D.J., Enright, R., and Wang, E.N. (2013). Electric-field-enhanced condensation on superhydrophobic nanostructured surfaces. ACS Nano *7*, 11043–11054.

19. Birbarah, P., Li, Z., Pauls, A., and Miljkovic, N. (2015). A comprehensive model of electric-field-enhanced jumping-droplet condensation on superhydrophobic surfaces. Langmuir *31*, 7885–7896.

20. Wen, R., Xu, S., Ma, X., Lee, Y.C., and Yang, R. (2018). Three-dimensional superhydrophobic nanowire networks for enhancing condensation heat transfer. Joule *2*, 269–279.

21. Hou, Y., Yu, M., Chen, X., Wang, Z., and Yao, S. (2015). Recurrent filmwise and dropwise condensation on a beetle mimetic surface. ACS Nano *9*, 71–81.

22. Ölçeroğlu, E., and McCarthy, M. (2016). Self-organization of microscale condensate for delayed flooding of nanostructured superhydrophobic surfaces. ACS Appl. Mater. Interfaces *8*, 5729–5736.

23. Boreyko, J.B., and Chen, C.H. (2010). Self-propelled jumping drops on superhydrophobic surfaces. Phys. Fluids *22*, 091110.

24. Liu, F., Ghigliotti, G., Feng, J.J., and Chen, C.H. (2014). Numerical simulations of self-propelled jumping upon drop coalescence on non-wetting surfaces. J. Fluid Mech. *752*, 39–65.

25. Enright, R., Miljkovic, N., Sprittles, J., Nolan, K., Mitchell, R., and Wang, E.N. (2014). How coalescing droplets jump. ACS Nano *8*, 10352–10362.

26. Mouterde, T., Nguyen, T.V., Takahashi, H., Clanet, C., Shimoyama, I., and Quéré, D. (2017). How merging droplets jump off a superhydrophobic surface: measurements and model. Phys. Rev. Fluids *2*, 112001.

27. Miljkovic, N., Enright, R., and Wang, E.N. (2013). Modeling and optimization of superhydrophobic condensation. J. Heat Transfer *135*, 111004.

28. Rykaczewski, K., Paxson, A.T., Anand, S., Chen, X., Wang, Z., and Varanasi, K.K. (2013). Multimode multidrop serial coalescence effects during condensation on hierarchical superhydrophobic surfaces. Langmuir *29*, 881–891.

29. Lv, C., Hao, P., Yao, Z., and Niu, F. (2015). Departure of condensation droplets on superhydrophobic surfaces. Langmuir *31*, 2414–2420.

30. He, M., Zhou, X., Zeng, X., Cui, D., Zhang, Q., Chen, J., Li, H., Wang, J., Cao, Z., Song, Y., et al. (2012). Hierarchically structured porous aluminum surfaces for high-efficient removal of condensed water. Soft Matter *8*, 6680–6683.

31. Wang, K., Li, R., Liang, Q., Jiang, R., Zheng, Y., Lan, Z., and Ma, X. (2017). Critical size ratio for coalescence-induced droplet jumping on superhydrophobic surfaces. Appl. Phys. Lett. *111*, 061603.

32. Wasserfall, J., Figueiredo, P., Kneer, R., Rohlfs, W., and Pischke, P. (2017). Coalescence-induced droplet jumping on superhydrophobic surfaces: effects of droplet mismatch. Phys. Rev. Fluids *2*, 123601.

33. Dietz, C., Rykaczewski, K., Fedorov, A.G., and Joshi, Y. (2010). Visualization of droplet departure on a superhydrophobic surface and implications to heat transfer enhancement during dropwise condensation. Appl. Phys. Lett. *97*, 033104.

34. Chen, X., Wu, J., Ma, R., Hua, M., Koratkar, N., Yao, S., and Wang, Z. (2011). Nanograssed micropyramidal architectures for continuous dropwise condensation. Adv. Funct. Mater. *21*, 4617–4623.

35. Boreyko, J.B., and Collier, C.P. (2013). Delayed frost growth on jumping-drop superhydrophobic surfaces. ACS Nano *7*, 1618–1627.

36. Chen, X., Weibel, J.A., and Garimella, S.V. (2015). Exploiting microscale roughness on hierarchical superhydrophobic copper surfaces for enhanced dropwise condensation. Adv. Mater. Interfaces *2*, 1400480.

37. Ölçeroğlu, E., Hsieh, C.Y., Rahman, M.M., Lau, K.K.S., and McCarthy, M. (2014). Full-field dynamic characterization of superhydrophobic condensation on biotemplated nanostructured surfaces. Langmuir *30*, 7556–7566.

38. Boreyko, J.B., and Chen, C.H. (2013). Vapor chambers with jumping-drop liquid return from superhydrophobic condensers. Int. J. Heat Mass Transf. *61*, 409–418.

39. Birbarah, P., and Miljkovic, N. (2017). External convective jumping-droplet condensation on a flat plate. Int. J. Heat Mass Transf. *107*, 74–88.

40. Furmidge, C.G.L. (1962). Studies at phase interfaces I. The sliding of liquid drops on solid surfaces and a theory for spray retention. J. Colloid Sci. *17*, 309–324.

41. Carey, V.P. (2007). Liquid Vapor Phase-Change Phenomena (CRC Press).

42. Enright, R., Miljkovic, N., Al-Obeidi, A., Thompson, C.V., and Wang, E.N. (2012). Condensation on superhydrophobic surfaces: the role of local energy barriers and structure length scale. Langmuir *28*, 14424–14432.

43. Rykaczewski, K. (2012). Microdroplet growth mechanism during water condensation on superhydrophobic surfaces. Langmuir *28*, 7720–7729.

44. Boreyko, J.B., Baker, C.H., Poley, C.R., and Chen, C.H. (2011). Wetting and dewetting transitions on hierarchical superhydrophobic surfaces. Langmuir *27*, 7502–7509.

45. Lafuma, A., and Quéré, D. (2003). Superhydrophobic states. Nat. Mater. *2*, 457–460.

46. Bormashenko, E., Pogreb, R., Whyman, G., Bormashenko, Y., and Erlich, M. (2007). Vibration-induced cassie-Wenzel wetting transition on rough surfaces. Appl. Phys. Lett. *90*, 201917.

47. Verho, T., Korhonen, J.T., Sainiemi, L., Jokinen, V., Bower, C., Franze, K., Franssila, S., Andrew, P., Ikkala, O., and Ras, R.H.A. (2012). Reversible switching between superhydrophobic states on a hierarchically structured surface. Proc. Natl. Acad. Sci. USA *109*, 10210–10213.

48. Boreyko, J.B., and Collier, C.P. (2013). Dewetting transitions on superhydrophobic surfaces: when are Wenzel drops reversible? J. Phys. Chem. C *117*, 18084–18090.

49. Enright, R., Miljkovic, N., Dou, N., Nam, Y., and Wang, E.N. (2013). Condensation on superhydrophobic copper oxide nanostructures. J. Heat Transfer *135*, 091304.

50. Qu, X., Boreyko, J.B., Liu, F., Agapov, R.L., Lavrik, N.V., Retterer, S.T., Feng, J.J., Collier, C.P., and Chen, C.H. (2015). Self-propelled sweeping removal of dropwise condensate. Appl. Phys. Lett. *106*, 221601.

51. Lv, C., Hao, P., Yao, Z., Song, Y., Zhang, X., and He, F. (2013). Condensation and jumping relay of droplets on lotus leaf. Appl. Phys. Lett. *103*, 021601.

52. Dorrer, C., and Rühe, J. (2007). Condensation and wetting transitions on microstructured ultra-hydrophobic surfaces. Langmuir *23*, 3820–3824.

53. Lv, C., Hao, P., Zhang, X., and He, F. (2015). Dewetting transitions of dropwise condensation on nanotexture-enhanced superhydrophobic surfaces. ACS Nano *9*, 12311–12319.

54. Viovy, J.L., Beysens, D.A., and Knobler, C.M. (1988). Scaling description for the growth of condensation patterns on surfaces. Phys Rev A Gen Phys. *37*, 4965–4970.

55. Zhao, H., and Beysens, D. (1995). From droplet growth to film growth on a heterogeneous surface: condensation associated with a wettability gradient. Langmuir *11*, 627–634.

56. Kim, S., and Kim, K.J. (2011). Dropwise condensation modeling suitable for

superhydrophobic surfaces. J. Heat Transfer *133*, 081502.

57. Nabavian, K., and Bromley, L.A. (1963). Condensation coefficient of water. Chem. Eng. Sci. *18*, 651–660.

58. Tanner, D.W., Potter, C.J., Pope, D., and West, D. (1965). Heat transfer in dropwise condensation—part I The effects of heat flux, steam velocity and non-condensable gas concentration. Int. J. Heat Mass Transf. *8*, 419–426.

59. Minkowycz, W.J., and Sparrow, E.M. (1966). Condensation heat transfer in the presence of noncondensables, interfacial resistance, superheating, variable properties, and diffusion. Int. J. Heat Mass Transf. *9*, 1125–1144.

60. Zhao, Y., Preston, D.J., Lu, Z., Zhang, L., Queeney, J., and Wang, E.N. (2018). Effects of millimetric geometric features on dropwise condensation under different vapor conditions. Int. J. Heat Mass Transf. *119*, 931–938.

61. Preston, D.J., and Wang, E.N. (2018). Jumping droplets push the boundaries of condensation heat transfer. Joule *2*, 205–207.

62. Boreyko, J.B., Polizos, G., Datskos, P.G., Sarles, S.A., and Collier, C.P. (2014). Air-stable droplet interface bilayers on oil-infused surfaces. Proc. Natl. Acad. Sci. USA *111*, 7588–7593.

JOUL, Volume *3*

Supplemental Information

How Surface Orientation Affects Jumping-Droplet Condensation

Ranit Mukherjee, Austin S. Berrier, Kevin R. Murphy, Joshua R. Vieitez, and Jonathan B. Boreyko

1 Finding Wenzel neck radius of impaled droplets:

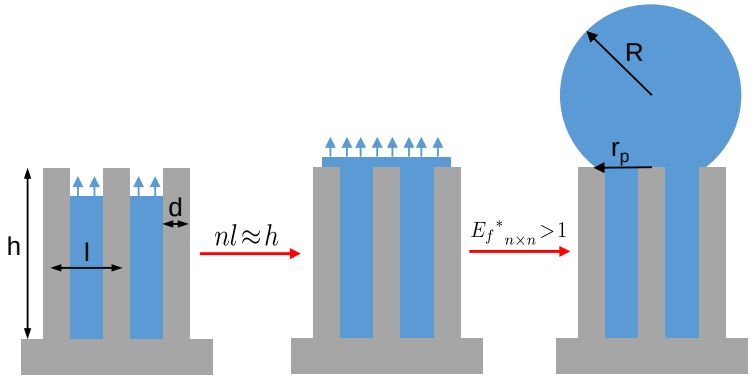

Figure S1: Schematic of droplet growth from the nano-cavities on the superhydrophobic surface used in the condensation experiments.

For determining the neck radius of an impaled droplet with Wenzel neck, we have followed the three-stage growth model developed by Mulroe et al [1]. Initially a nanometric droplet nucleates within the pillars and grows by direct condensation. In the first stage of the model, we compare the energy required for lateral expansion to adjacent unit cells ($\Delta E_{i,s}$) and for upward droplet growth to reach the pillar top of the current unit cell ($\Delta E_{i,u}$). For a droplet constrained by $n \times n$ unit cells, this energy comparison can be written as a ratio-

$$(\Delta E_i{}^*)_{n\times n} = \frac{(\Delta E_{i,s})_{n\times n}}{(\Delta E_{i,u})_{n\times n}} = \frac{(l-d)(1-\cos\theta_a) - 2nl\cos\theta_a}{4(l-d) - n\pi d\cos\theta_a}. \tag{1}$$

A droplet will preferentially grow upward if either $\Delta E_i{}^*$ is greater than 1 or the height of the droplet reaches the pillar tops ($nl \approx h$) before $\Delta E_i{}^* > 1$. With our specific surface geometries, $nl \approx h$ was first satisfied for $n = 5$. Thus, the constrained droplet will grow laterally within 5 unit cells before reaching pillar tops. In the second stage, the droplet now flushed with the pillar tops can either grow sideways or can inflate upward as a Cassie droplet. An energy comparison similar to stage 1 can be used to find out the energetically favorable mode of growth-

$$(\Delta E_f{}^*)_{n\times n} = \frac{(\Delta E_{f,i})_{n\times n}}{(\Delta E_{f,u})_{n\times n}} = \frac{(nl-d)(1-\cos\theta_a) - 2nh\cos\theta_a}{n\pi l}. \tag{2}$$

For our surface, $\Delta E_f{}^* > 1$ is immediately satisfied for the $n = 5$ value obtained from stage 1. Thus as soon as the droplet reaches the pillar tops, it will grow upward. This critical value of n can now be used to find out the neck radius r_p as depicted in Figure 1. The neck radius is found out to be $r_p \approx 0.5nl = 297.5$ nm for our surface.

2 Model of coalescence-induced impalement:

In the main manuscript, the theoretical model assumed that coalescence caused droplet detachment and/or departure from the surface. However, it should also be considered whether coalescence could induce the opposite effect, namely, impalement into the texture. There are three possible mechanisms for coalescence-induced impalement: i) the excess surface energy is much higher than the merged droplet's work of cohesion, such that only a portion of the droplet rips off the impaled necks, ii) the Wenzel state is more favorable than the Cassie state, or iii) the dynamic pressure exerted by the liquid bridge during coalescence exceeds the Laplace pressure required to invade the nanopillars. Each of these will now be considered in turn.

The work of cohesion to break the merged droplet into two pieces is $W_c \approx 2\gamma A$, where A is the surface area of the merged droplet. From volume conservation, $A = 2^{\frac{4}{3}}\pi R^2(2 - 3\cos\theta_{app} + \cos\theta_{app}{}^3)^{\frac{2}{3}}$. With $\theta_{app} = \theta_{adv} \approx 160^\circ$ and initial droplet radius, R= 867 μm we find that $W_c \approx 10^{-6}$. As the work of adhesion to detach two droplets from their respective Wenzel necks ($\Delta E_{ad|N}$) is considerably lower than the work of cohesion, the excess surface energy released during coalescence would first supply the energy required for droplet detachment from the impaled neck before supplying energy for breaking up the merged droplet.

If the Cassie state were merely metastable, then the energy released by coalescence could overcome the energy barrier to switch to the more stable Wenzel state. The Cassie state is energetically favorable over the Wenzel state when [2]:

$$\theta_c = \cos^{-1}\left(\frac{\phi - 1}{r - \phi}\right). \tag{3}$$

With $\phi = 0.295$ as the solid fraction and $\theta_a \approx 113^\circ$, we find that $\theta_c = 94.6^\circ$ which indicates that the Cassie state is energetically more favorable in our surface.

During coalescence, a liquid bridge rapidly expands against the substrate due to symmetry breaking. The dynamic pressure due to bridging (ΔP_d) can be approximated by $\rho {v_b}^2$, where $v_b \approx 2{D_0}^2(\gamma/\rho R)^{1/2}$ is the bridging velocity and $D_0 \approx 1.62$ is a prefactor found from numerical simulations [3]. The capillary pressure barrier (ΔP_c) is scaled as $|2\gamma cos\theta_{app}|/p$, where p is the pitch distance between the nanopillars. With $p = 119$ nm, we found that ΔP_c is three orders of magnitude higher than ΔP_d for any micrometric droplets. Thus, in the modeling of the coalescence-induced droplet rolling, we can neglect the work of cohesion or impalement of the merged droplet after coalescence and only compare the excess surface energy of coalescence with the work of adhesion required to detach the merged droplet from the nanostructures.

3 Condensation heat transfer coefficient model:

For a condensing superhydrophobic surface, droplet size distribution $n(r)$ for non-interacting droplets is given by [4]:

$$n(r) = \frac{1}{3\pi {r_{col}}^3 r_{max}} \left(\frac{r_{col}}{r_{max}}\right)^{-2/3} \frac{r(r_{col} - r_{min})}{r - r_{min}} \frac{A_2 r + A3}{A_2 r_{col} + A_3} exp(B_1 + B_2) \tag{4}$$

and for droplets bigger than the coalescence radius, the droplet size distribution, $N(r)$ is simply given by:

$$N(r) = \frac{1}{3\pi r^2 r_{max}} \left(\frac{r}{r_{max}}\right)^{-2/3} \tag{5}$$

Here the constants B_1 and B_2 can be further defined as-

$$B1 = \frac{A2}{\tau A1} \left[\frac{{r^2}_{col} - r^2}{2} + r_{min}(r_{col} - r) - {r^2}_{min} ln\left(\frac{r - r_{min}}{r_{col} - r_{min}}\right)\right]$$

$$B2 = \frac{A3}{\tau A1} \left[r_{col} - r - r_{min} ln\left(\frac{r - r_{min}}{r_{col} - r_{min}}\right)\right]$$

with the sweeping period, τ expressed as-

$$\tau = \frac{3 r_{col}^2 (A_2 r_{col} + A_3)^2}{A_1 (11 A_2 r_{col}^2 - 14 A_2 r_{col} r_{min} + 8 A_3 r_{col} - 11 A_3 r_{min}}$$

and A_1, A_2, A_3 are denoted by-

$$A1 = \frac{\Delta T}{\rho h_{fg} (1 - \cos\theta)^2 (2 + \cos\theta)}, A2 = \frac{\theta}{4 k_w \sin\theta}$$

$$A3 = \frac{1}{2h_i(1 - \cos\theta)} + \frac{1}{k_c \sin^2\theta} \left[\frac{k_p \phi}{\delta_c k_p + h k_c} + \frac{k_w (1 - \phi)}{\delta_c k_w + h k_c}\right]^{-1} \tag{6}$$

Here, r_{col} is the coalescence radius above which droplet growth occurs mainly by coalescence. In general, the coalescing length-scale can be optimized by surface structure design. For our surface, this coalescing lengthscale is assumed to be 1 μm which is similar to the coalescing and deparing size observed on an equivalent surface by Mulroe et al. r_{min} is the critical nucleation radius of the condensing droplets on a structured surface which can be taken as 10 nm for water in ambient conditions [5]. The upper bound of the droplet distribution, r_{max} is the maximum droplet radius on the surface. In all previous jumping-droplet heat transfer models it was considered constant as the departure radius of the droplets does not depend on surface inclination in jumping droplet condensation. But even though the critical jumping droplet size is dependent on the surface structures only, the orientation of the surface ultimately controls the maximum droplet size on the surface for long-time condensation. So, in our model, r_{max} is varied within a range of 10 μm to 900 μm, which includes the maximum droplet size seen on our surfaces in our experiments for all three orientations. A key point to note here is that for pure jumping droplet condensation the

droplet sweeping is non-existent or the sweeping period, τ is infinite. But, as seen in our experiments, during long term condensation, the surface shows both jumping and sweeping removal of condensing droplets. In such cases the sweeping terms B_1 and B_2 can not be neglected. In Figure 2, we have compared the heat transfer coefficient with and without sweeping term. As the difference is not substantially large and both of the curves are qualitatively similar, we have neglected the sweeping term in our model.

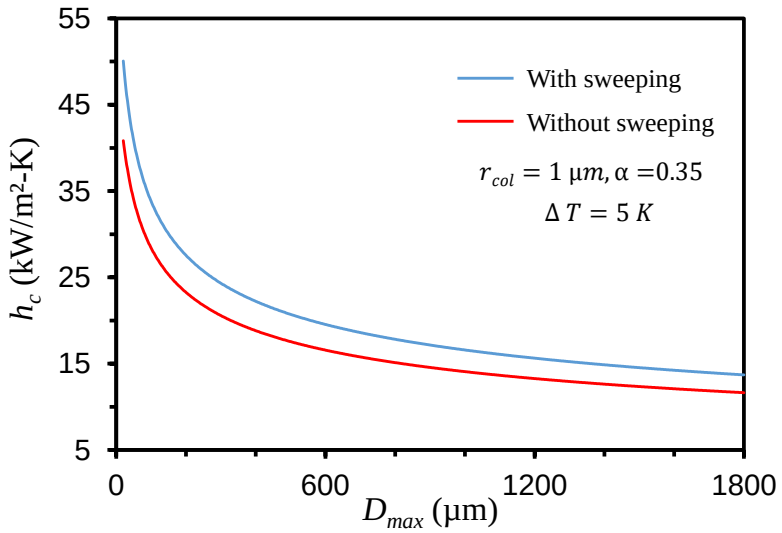

Figure S2: Effect of sweeping on the condensation heat transfer coefficient. If all other variables are kept constant, the surface with sweeping shows slightly better heat transfer performance. As the two curves are qualitatively same, we have used the model with no sweeping in the main paper.

Supplemental References

[1] M. D. Mulroe, B. R. Srijanto, S. F. Ahmadi, C. P. Collier, and J. B. Boreyko. Tuning superhydrophobic nanostructures to enhance jumping-droplet condensation. *ACS Nano*, 1:8499—8510, 2017.

[2] A. Lafuma and D. Quéré. Superhydrophobic states. *Nat. Mater.*, 2:457–460, 2003.

[3] J. Oh, R. Zhang, P. P. Shetty, J. A. Krogstad, P. V. Braun, and N. Miljkovic. Thin film condensation on nanostructured surfaces. *Adv. Funct. Mater.*, 1707000:1–10, 2018.

[4] N. Miljkovic, R. Enright, and E. N. Wang. Modeling and optimization of superhydrophobic condensation. *J. Heat Transfer*, 135:111004, 2013.

[5] V. P. Carey. *Liquid–Vapor Phase-Change Phenomena, 2nd ed.* CRC Press, Boca Raton, FL, 2007.